**Proceedings of the ASME 2022 41st International Conference on Ocean, Offshore and Arctic Engineering
OMAE2022
June 5-10, 2022, Hamburg, Germany**

OMAE2022-78157

MARINE DUCTED THRUSTER UNDERWATER RADIATED NOISE CONTROL THROUGH LEADING-EDGE TUBERCLE BLADE MODIFICATIONS - A NUMERICAL HYBRID APPROACH

Callum Stark
Department of Naval Architecture, Ocean and Marine Engineering, University of Strathclyde, Glasgow, UK

Weichao Shi
Department of Naval Architecture, Ocean and Marine Engineering, University of Strathclyde, Glasgow, UK

Yunxin Xu
Department of Naval Architecture, Ocean and Marine Engineering, University of Strathclyde, Glasgow, UK

Moritz Troll
Department of Naval Architecture, Ocean and Marine Engineering, University of Strathclyde, Glasgow, UK

ABSTRACT

Anthropogenic-related underwater radiated noise (URN) has a detrimental impact on marine creatures who utilise the acoustic environment to perform basic living functions. Ambient ocean noise levels are increasing due to the growth of global shipping activity, where the propeller under cavitating conditions typically dominates the URN signature of marine vessels. Therefore, reducing cavitation severity and the subsequent URN is critical for future marine craft. This paper aims to assess the noise mitigation capability of LE tubercles on a benchmark Kaplan-type ducted propeller blade in cavitating conditions using computational fluid dynamics (CFD), detached eddy simulations (DES) are implemented to solve the hydrodynamic flow-field and the Schnerr-Sauer model is used to describe the cavitation behaviour. Both near and far-field noise is predicted within the hydroacoustic analysis. The Ffowcs-Williams Hawkings (FW-H) acoustic analogy was utilised to propagate the generated noise into the far-field. In summary, it was found that the LE tubercle modified ducted propeller blades could produce a noise reduction in the far-field at most test conditions considered to a maximum of 6dB overall average sound pressure level (OASPL). This is believed to be predominantly due to the introduction of the counter-rotating vortex pairs and subsequent alteration of the local pressure field over the blade suction side, which ultimately reduces the sheet cavitation severity over the blade surface by funnelling the cavitation behind the tubercle trough region.

Keywords: Leading-edge tubercles, ducted propeller, underwater radiated noise, FW-H acoustic analogy

1. INTRODUCTION

Anthropogenic-related underwater radiated noise (URN) has a negative impact on marine creatures that use the acoustic environment to perform basic living functions such as navigating and catching prey [1]. Ocean noise levels are believed to be increasing because of the rapid growth of global shipping activity [2]. Due to this, the International Maritime Organization (IMO) published non-mandatory guidelines in 2014 to encourage the reduction of shipping-related underwater noise pollution [3]. However, there is a lack of rules and regulations exclusively dedicated to shipping URN control [4]. Nonetheless, it is expected that URN will be a key early design factor for future vessel design, therefore URN reduction designs must be developed.

Shipping-related URN is generally dominated by the propeller, especially when the propeller is operating in cavitating conditions [5]. Cavitation is an undesirable phenomenon as it can cause performance degradation, erosion and increased vibration and URN [6]. Therefore, mitigating propeller cavitation is a critical area of research when considering the reduction of URN.

A marine mammal negatively affected by anthropogenic noise could be the answer to our problems. The humpback whale (*megaptera novaeangliae)* can perform acrobatic manoeuvres to catch prey despite its large build. This ability is aided by the small bumps or leading-edge (LE) tubercles located on the pectoral fins of the mammal [7]. LE tubercles have been researched on applications such as aero/hydrofoils, tidal turbines, rudders and marine propulsors [8-16]. LE tubercles produce counter-rotating vortex pairs which can influence the local flow-field, and the tubercle modifications have shown to alter the cavitation development on a variety of applications. Custodio et al. [9] conducted an experimental investigation into the performance of hydrofoils in the presence of cavitation. It was concluded that the leading-edge modified hydrofoils directed the cavitation behind the troughs whereas the baseline hydrofoil produced cavitation along its entire leading-edge. Weber et al. [10] used experimental methods to investigate the effect of LE tubercles on the lift, drag and cavitation onset of rudders operating at low Reynold's numbers. It was concluded that the inclusion of LE tubercles compartmentalised the cloud cavitation into slots in the troughs. Shi et al. [11] established the concept onto tidal turbines. An in-depth numerical and experimental study was conducted into the feasibility of LE tubercles on such a device. The investigation showed that cavitation can be contained and URN levels can be reduced in certain operating conditions.

More recently, LE tubercles have been applied to open and ducted propellers blades, as well as the duct [12-16]. Using CFD, Stark and Shi [13] showed that tubercle modified marine propellers could enhance hydrodynamic efficiency under heavy-cavitating conditions while the tubercles induced a cavitating fencing pattern, confining the sheet cavitation to behind the trough regions which resulted in a reduction in cavitation volume. Stark et al. [16] investigated the influence of LE tubercles modified blades on a typical ducted propeller design using CFD, showing that under the same thrust loading in heavy-cavitating conditions, the LE tubercle ducted propeller could enhance the hydrodynamic efficiency by 6.5%. A cavitation funnelling effect was observed across the blade surface, which resulted in a cavitation volume reduction of over 50%. In addition, the pressure pulse fluctuations in the near-field were predicted to be reduced in certain conditions, which is a strong indication of a reduction in URN.

In light of this, this study is an extension of previous work, where the influence of LE tubercle blade modifications on the URN signature of a benchmark ducted propulsor in cavitating conditions is investigated. A numerical hybrid approach is employed, whereby the hydrodynamic flow-field is solved using detached eddy simulations (DES) and the Ffowcs Williams-Hawkings (FW-H) acoustic analogy is used to propagate the g enerated noise into the far-field.

2. TEST CASE

2.1 Overview

a) REF b) TUB

FIGURE 1 : DUCTED PROPELLER GEOMETRY

The reference geometry 'REF' was selected as the benchmark 19A ducted propeller and Kaplan series, KA4-55 propeller, detailed geometry can be found in Carlton [6]. The rendered geometry can be found in Figure 1 and the parameters in Table 1. The tubercle blade design was idealised as a sinusoidal waveform with a height, H of $0.1c$ and wavelength, λ, $0.5c$ where c is the local chord length.

TABLE 1: GEOMETRICAL PARAMETERS OF REFERENCE DUCTED PROPELLER

Variable (Duct)	Unit	Variable (Propeller)	Unit
Type	19A	**Type**	Kaplan
Outer Diameter, D_d	306mm	**Blade number**	4
Inner diameter, D_i	254mm	**Expanded Area Ratio (EAR)**	0.55
Chord, L_{DUCT}	125mm	**Pitch-diameter Ratio (P/D)**	1
		Diameter, D	250mm
		Tip Clearance, t	2mm
		Position wrt Duct	$0.5L_{DUCT}$

2.2 Computational Domain

The computational domain consisted of a cylindrical domain, where the propeller centre was located $4D$ from the inlet and $10D$ from the outlet and $4D$ from the outer circumferential wall. The inlet was defined as a velocity inlet, outlet as pressure outlet and symmetry plane on the circumferential face as shown in Figure 2. The duct and propeller were defined as no-slip wall boundaries. The propeller rotation was achieved by creating a rotating region separate from the rest of the domain (static region).

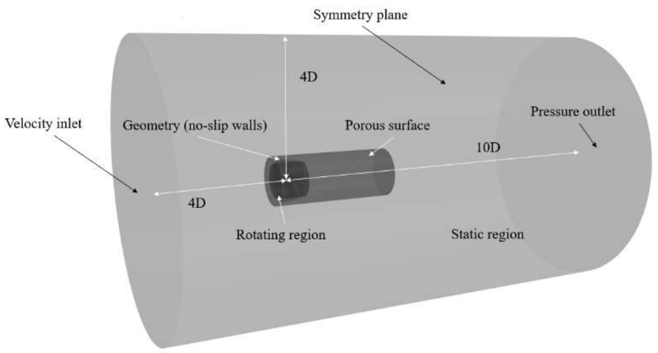

FIGURE 2 : COMPUTATIONAL DOMAIN

2.3 Mesh Generation

The mesh was generated using unstructured hexahedral mesh to the count of approximately 13 million cells. A low y^+ wall approach was employed, where a fine prism layer mesh was used to resolve the boundary layer. An average $y^+ <1$ was achieved and a maximum y^+ of roughly 2.3 was located on the blade leading-edge. A volumetric control was selected to align with the porous region to maintain a uniform mesh which can reduce the level of numerical diffusion due to change in mesh cell size in the porous region [17]. The blade and duct surface mesh can be seen in Figure 3 and a section of volume mesh can be seen in Figure 4 denoting the mesh refinement region inside the porous surface.

FIGURE 3: SURFACE MESH

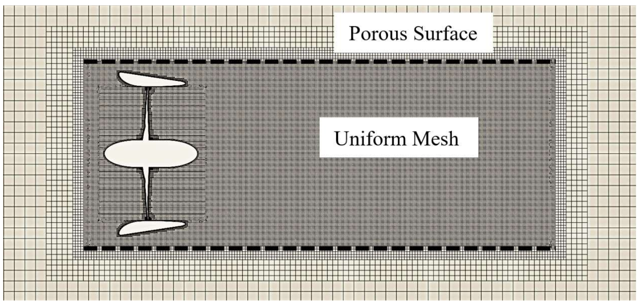

FIGURE 4: CUT-SECTION VOLUME MESH

2.4 Permeable Surface Design

The porous surface was 0.7*D* from the propeller plane and 3.5*D* in length to allow for a portion of the turbulent wake structure to be accounted for within the noise prediction. The end-caps were also removed from the porous surface. The porous surface and the near-field receiver position can be shown in Figure 5 and can be described in terms of x, y and z coordinates and normalised by the propeller diameter, *D*, with the origin of the domain located at the propeller centre. Far-field receivers were located at 100*D* from the propeller and at increments of 30º to cover the 360º range, this can seen in Figure 6.

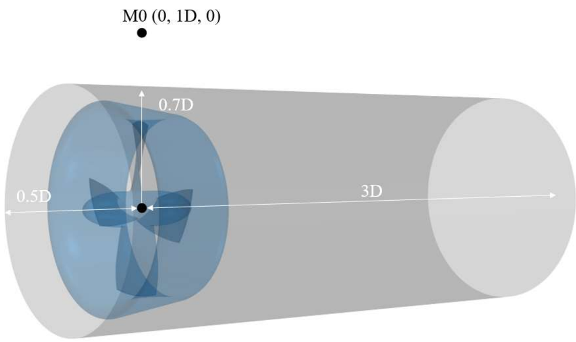

FIGURE 5: POROUS SURFACE AND NEAR-FIELD RECEIVER POSITION (M0)

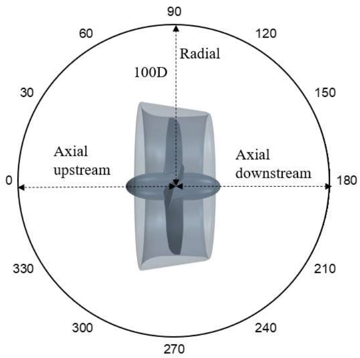

FIGURE 6: FAR-FIELD RECEIVER POSITIONS

3. NUMERICAL APPROACH

3.1 Hydrodynamic and Hydroacoustic Modelling

The hydrodynamic flow field was solved using the implicit unsteady Improved Delayed Detached Eddy Simulation (IDDES) solver from commercial code STAR CCM+, which has been used extensively for a wide array of maritime problems. The sliding mesh technique was implemented for the transient analysis. Firstly, the flow field was initialised using the single-phase flow solver to allow for more robust convergence when the multiphase flow interaction was present, i.e. cavitation. Then, the multiphase flow model was introduced to allow cavitation to occur. In non-cavitating conditions, the propeller ran for approximately 8 revolutions to determine key variables thrust

and torque. To obtain the open-water curve, the propeller rotational rate, n, was fixed at 15rps, while the advance velocity, V_A, was varied. The Reynolds number, Rn can be estimated as 1x10^6 based on the rotational rate.
In cavitating conditions, the propeller ran for approximately 16 revolutions where key variables had stabilised such as the thrust, torque, cavitation volume and near-field hydrodynamic pressure and then the acoustic data was collected from the latter 8 revolutions. The Ffowcs-Williams Hawkings (FW-H) acoustic analogy was utilised to propagate the generated noise into the far-field, both linear and non-linear noise sources were considered by employing a porous surface approach. The convective and temporal terms in the momentum equations were discretised with a 2nd order scheme. The equations were coupled by using a segregated SIMPLE type solution algorithm. The SST k-omega turbulence model was used. The time-step used was 1 degree of rotation per time-step, a time-step of between 0.5 and 2 degrees is recommended by ITTC [18].

Acoustic pressure is collected in the time domain at each time step. By using FFT (Fast Fourier Transform), it is transferred to the frequency domain and then sound pressure level (SPL) values are calculated in the frequency domain as follows in Eqn 1:

$$SPL = 20log\left(\frac{p}{p_{ref}}\right) \tag{1}$$

Here, p is acoustic pressure in the frequency domain, Pa, p_{ref}, is reference acoustic pressure, Pa (for water p_{ref}=1x10^{-6} Pa). In addition, overall sound pressure level (OASPL) is calculated by Eqn 2:

$$OASPL = 20\log\left(\frac{P_{rss}}{P_{ref}}\right) \tag{2}$$

where P_{rss} is total acoustic pressure, Pa, which is obtained within this study by summing the acoustic pressures in the 3rd octave band frequency domain in accordance with root sum square (RSS) rule.

3.2 Cavitation Model

The multiphase flow was modelled using the volume of fluid (VOF) model and the cavitation behaviour was described using the Schnerr-Sauer model. The Schnerr-Sauer model is based on the reduced Rayleigh-Plesset equation, and neglects the influence of bubble growth acceleration, viscous effects, and surface tension. Nonetheless, this cavitation model has provided good agreement with experimental sheet cavitation observations and noise measurements [19]. The cavitation number, σ_N, can be described in Eqn 3.

$$\sigma_N = \frac{P_0 - P_v}{\frac{1}{2}\rho(nD)^2} \tag{3}$$

where P_0 is the static pressure including the atmospheric pressure, Pa, Pv is the vapour pressure of the water, Pa. n is the rotational speed, rps, ρ is the water density, kg/m^3, D is propeller diameter, m. Table 2 shows the test conditions considered within the analysis, where C1-C3 denotes heavy-cavitating conditions and C4-C6 denotes light-cavitating conditions. Advance ratio, J is defined as shown in Eqn. 4.

$$J = \frac{V_A}{nD} \tag{4}$$

TABLE 2: TEST CONDITIONS CONSIDERED WITHIN NUMERICAL ANALYSIS

Condition, C	V_A (m/s)	n (rps)	Rn	J	σ_N
C1	0.375	15	1.05x10^6	0.1	1.3 (Heavy)
C2	1.125			0.3	
C3	2.0625			0.55	
C4	0.375			0.1	1.9 (Light)
C5	1.125			0.3	
C6	2.0625			0.55	

4. VERIFICATION AND VALIDATION

4.1 Performance Coefficients

The performance of the marine propeller follows the traditional open-water curve characteristics. The variables for propeller, duct and total thrust, K_{TP}, K_{TD}, and K_{TT}, torque, K_Q and efficiency, η can be described in Eqns. 5-9, respectively.

$$K_{TP} = \frac{T_P}{\rho n^2 D^4} \tag{5}$$

$$K_{TD} = \frac{T_D}{\rho n^2 D^4} \tag{6}$$

$$K_{TT} = K_{TP} + K_{TD} \tag{7}$$

$$K_Q = \frac{Q}{\rho n^2 D^5} \tag{8}$$

$$\eta = \frac{K_{TT}J}{2\pi K_Q} \tag{9}$$

Where T_P and T_D are propeller and duct thrust, N, Q is propeller torque, Nm, and ρ, is density, kg/m^3.

4.2 Mesh Convergence

A verification study was conducted to determine the uncertainty of the numerical simulations. This was completed using the grid convergence index (GCI) method. The full methodology implemented in this study was defined by Celik et al [20] and can be found within. The total thrust and torque coefficient were selected as the integral variable at advance ratio, J = 0.55. The tabulated results can be shown in Table 3. The difference between the solution scalars (ε) is determined by Eqn. 10.

$$\varepsilon_{21} = \varphi_2 - \varphi_1,\ \varepsilon_{32} = \varphi_3 - \varphi_2, \qquad (10)$$

where, φ_1, φ_2 and φ_3 represent the results using fine (13 million cells), medium (7 million cells) and coarse (3 million cells) mesh grids, respectively. The ratio of solution scalars is used to calculate the convergence condition by Eqn. 11.

$$R = \frac{\varepsilon_{21}}{\varepsilon_{32}} \qquad (11)$$

Solution type is determined with respect to the convergence condition, R: 1. oscillatory convergence, $-1<R<0$; 2. monotonic convergence $0<R<1$; 3. oscillatory divergence $R<-1$; and 4. monotonic divergence, $R>1$, If R is found as in case 2, the procedure can be directly employed. GCI index is calculated by the following in Eqn. 12:

$$GCI_{fine}{}^{21} = \frac{1.25{e_a}^{21}}{{r_{21}}^{p} - 1} \qquad (12)$$

Here, p is apparent order, e_a is an approximate relative error. Detailed information about the verification procedure can be found in [20]. Results obtained for the thrust and torque coefficient and uncertainty level for both propeller geometries at J = 0.55 are given in Table 3. The convergence condition (R) was between 0 and 1 (monotonic convergence). As a result, the fine mesh, 13 million cells, was selected for future analysis.

TABLE 3: UNCERTAINTY ANALYSIS OF REF AT J = 0.55

	φ_1	φ_2	φ_3	R	$GCI_{FINE}\%$
K_{TT}	0.178	0.177	0.172	0.13	0.23
$10K_Q$	0.279	0.278	0.276	0.33	0.83

4.3 Hydrodynamic Validation with Experimental Test

Experimental data acquired by an internal test campaign at CTO, Poland using a KA4-55 and 19A duct was compared with the current numerical results. The description of the geometry can be shown in Figure 1 and was replicated in the computational domain. Figure 7 shows the results acquired from the open-water curve characteristics and good agreement can be seen between numerical and experimental results.

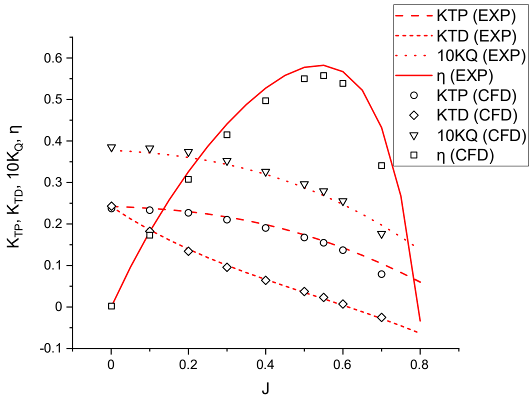

FIGURE 7: KA4-55 + 19A VALIDATION WITH EXPERIMENTAL TEST

4.4 Cavitation Observation Validation with Experimental Test

The experimental cavitation observations of the KA4-70 + 19A were used for validation of the numerical cavitation modelling. A selection of the cavitation observations can be found in [21]. The cavitation observation at J = 0.2 and σ_N = 1.9 in the test campaign was compared to the numerical results acquired at the same operating conditions and can be shown in Figure 8. The numerical cavitation visualization was achieved by using an iso-surface of the vapour fraction (α = 0.1). As can be seen, there is a good agreement between experimental and numerical cavitation observations.

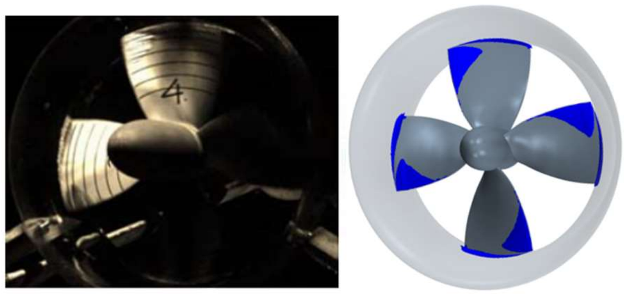

FIGURE 8: NUMERICAL CAVITATION OBSERVATIONS (PRESENT STUDY) COMPARED TO EXPERIMENTAL DATA FOR KA4-70 +19A ACQUIRED FROM [21] AT J = 0.2, σ_N= 1.9

4.5 Validation of FW-H Acoustic Analogy

To validate the FW-H acoustic analogy, the near-field direct hydrodynamic and hydroacoustic pressures were compared for the KA4-55 open propeller at the radial receiver, M0. This has been conducted in numerous studies within the literature for validation of the FW-H acoustic analogy [22] . As can be shown in Figure 9, there is good agreement between the direct hydrodynamic (DES) and hydroacoustic (FW-H) pressure.

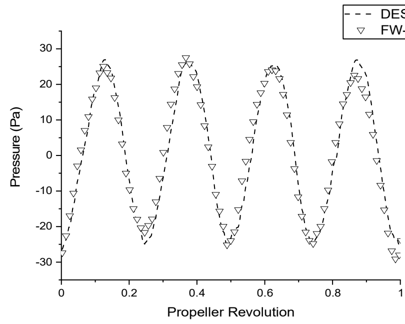

FIGURE 9: NEAR-FIELD HYDRODYNAMIC AND HYDROACOUSTIC PRESSURE FOR OPEN KA4-55 PROPELLER AT 1D FROM PROPELLER CENTRE IN RADIAL POSITION (M0) AT J = 0.55 IN NON-CAVITATING CONDITIONS

5. RESULTS

5.1 Cavitation Observations

Figure 10a shows the time-averaged cavitation volume predicted at conditions C1-C6 for both designs. Figure 10b shows the percentage reduction in time-averaged cavitation volume when comparing the TUB against the REF design. At all test conditions considered, the TUB design induced less sheet cavitation across the blades than when compared to the REF design, up to a maximum of roughly 50% reduction at C4. The sheet cavitation reduction over the blade surface is due to the introduction of the streamwise vortex pair (as shown in Figure 11) and containment of the low-pressure region (see Figure 12) over the suction side of the blade surface by the LE tubercle modification, which funnels the cavitation into the tubercle trough and encourages a cavitation-free zone behind the tubercle peaks with varying control depending on the operating condition.

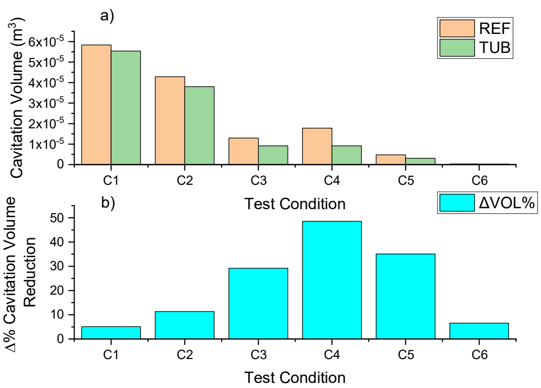

FIGURE 10: A) TIME-AVERAGED CAVITATION VOLUME B) PERCENTAGE REDUCTION OF TIME-AVERAGED CAVITATION VOLUME AT C1-C6

5.2 Hydrodynamic Performance

Figure 13 shows the time-averaged percentage difference in key performance coefficients between TUB and REF designs. Generally, the propeller thrust also improves (by a maximum of 10%), a reduction in thrust was observed at C4 and C5 by the TUB design. This is believed to be due to the cavitation being focused into a region of the blade (around 70% of the blade radius) that contributes a larger portion of overall propeller thrust as opposed to closer to the unloaded tip region (see Figure 11 and Figure 12). Nonetheless, the total thrust at each condition improves to a maximum of 10% while the propulsive efficiency improves by a maximum of 3.1% when compared at the same J.

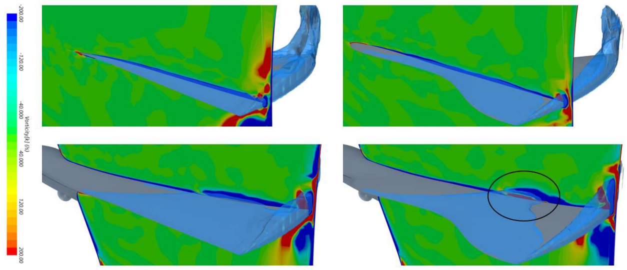

FIGURE 11: CAVITATION VOLUME AND PLANE-SECTION OF STREAMWISE VORTICITY AT TWO DIFFERENT LOCATIONS ACROSS THE BLADE SPAN FOR REF AND TUB DESIGNS AT C4

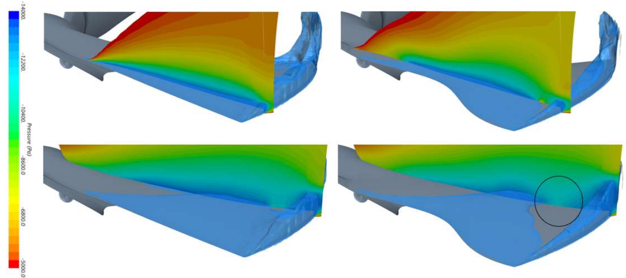

FIGURE 12: CAVITATION VOLUME AND PLANE-SECTION OF PRESSURE AT TWO DIFFERENT LOCATIONS ACROSS THE BLADE SPAN FOR REF AND TUB DESIGNS AT C4

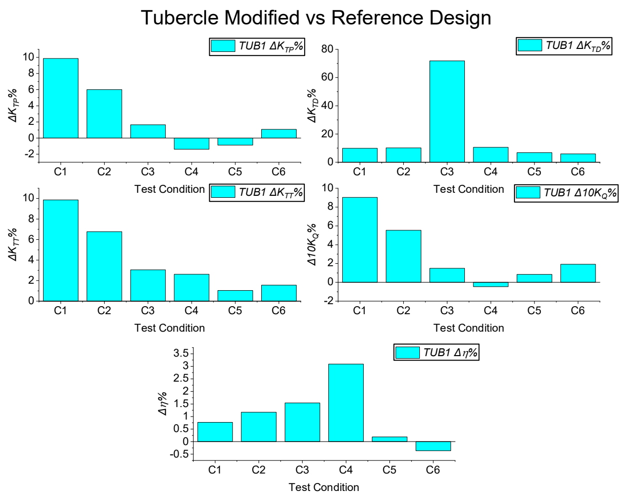

FIGURE 13: PERCENTAGE CHANGE IN TIME-AVERAGED KEY PERFORMANCE VARIABLES DUE TO LE TUBERCLE MODIFIED DUCTED PROPELLER BLADES

5.3 Near-Field Noise

Figure 14 shows the narrowband SPL spectra for C1-C6 at near-field pressure receiver M0. The 1st blade passage frequency (BPF) can be clearly observed at 60s^{-1} in all conditions, although less so in conditions C1-C4, at J= 0.1, where the blade loading is the highest. At C1, a noise reduction of roughly 5dB is observed below 100s^{-1}. At C4, a clear noise reduction below 1000s^{-1} is observed between 5-10dB. At C5 there is a general noise reduction across the whole frequency range, while at C6, there is no appreciable difference in SPL across the frequency range.

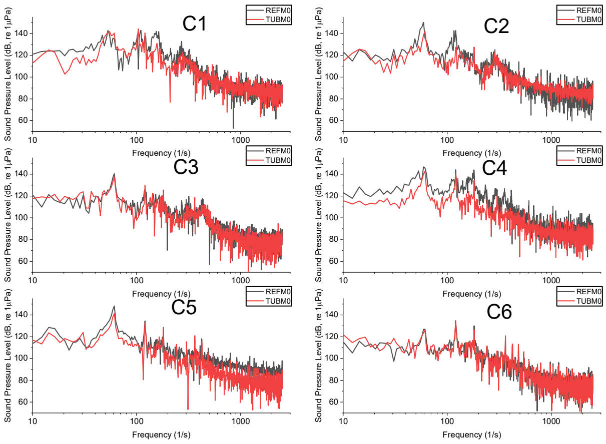

FIGURE 14: NEAR-FIELD NARROWBAND SPL SPECTRA FOR CONDITIONS C1-C6

5.4 Far-Field Noise

Figure 15 shows the 3rd octave band SPL plots of both ducted propeller designs at far-field location 90°, which is located at 100 propeller diameters (100D) away from the propeller centre in the radial direction from the propeller plane. Both designs at all cavitating conditions considered show similar spectrums regardless of the receiver position in the far-field. At condition C1, there is a reduction in noise in the mid-frequency range of approximately a maximum of 5dB with an increase in noise at the low and high frequency range of approximately 2.5dB. There is a clear noise reduction across most of the frequency range considered at C2 of a maximum 5dB, apart from the low frequency range of 0-30s^{-1} where an approximate increase of 5dB is shown. At condition C3, the TUB design produces less noise than the REF design across the frequency range, although this is marginal at approximately 1-2dB. At C4, the TUB design produces a reduction in noise across most of the frequency range by a maximum of 5dB apart from in the 0-30s^{-1} range, where an increase of 10dB is visible. The peak SPL is observed by the TUB design in the 0-30s^{-1} at C4 for all receivers which dominates the spectrum. At C5, a reduction of approximately 5dB is observed in the low-frequency range by the TUB design, with a slight increase across the rest of the spectrum. Figure 16 shows the change in SPL over the frequency spectra between REF and TUB design, where a positive y-value denotes a noise reduction due to the TUB design. Generally, the TUB provides a noise reduction across C1-C6 across most of the frequency range. A maximum reduction of 14dB is observed between 100 and 200s^{-1} at C1.

The OASPL directivity plots are shown in Figure 17. In conditions C2-C6, there is a reduction in OASPL at all directions considered to a maximum of roughly 6dB at C5. Therefore, in the above conditions, noise can be mitigated while simultaneously improving total thrust. This is also the case with propulsive efficiency except for C6. At C1 and C4 where both conditions were at the heaviest-loaded condition considered, J = 0.1, the OASPL increased by a maximum of 3.5dB. This is due to the increase in the low-frequency noise as shown in the 3rd octave band plots (see Figure 15) which is the source of the peak SPL across the spectrum and therefore, has a dominant weighting when calculating OASPL. Therefore, although cavitation volume is reduced at conditions C1 and C4 in the heavy-loaded condition (J = 0.1) and the near-field frequency spectrums show a clear noise reduction, the far-field noise OASPL shows an increase in noise due to the increase in peak SPL in the low-frequency range. If for example, the 0-100s^{-1} range was omitted from the OASPL calculation for C1 and C4 the reduction would be 3 and 7dB OASPL, respectively.

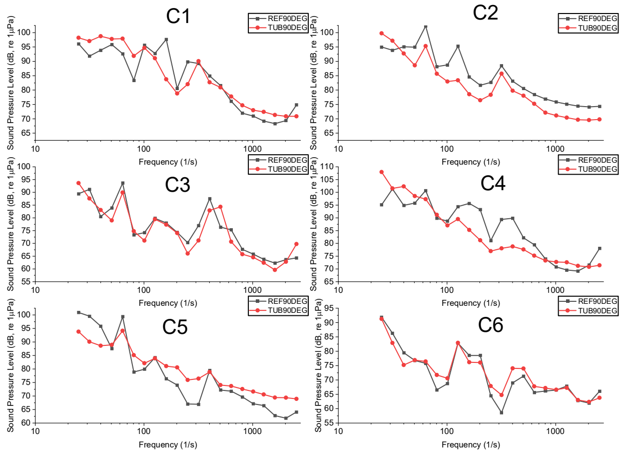

FIGURE 15: FAR-FIELD 3RD OCTAVE BAND SPL SPECTRA FOR CONDITIONS C1-C6

6. CONCLUDING REMARKS

In summary, a reduction of 6dB OASPL was observed in the far-field due to the LE tubercle blade modifications through a hybrid numerical approach (DES + FW-H). This was because the tubercle modification reduced the sheet cavitation severity across the blade surface, due to an introduction of a streamwise vortex pair and subsequent alteration of the local pressure field funneling cavitation behind the trough and encouraging cavitation-free zones behind the peak.

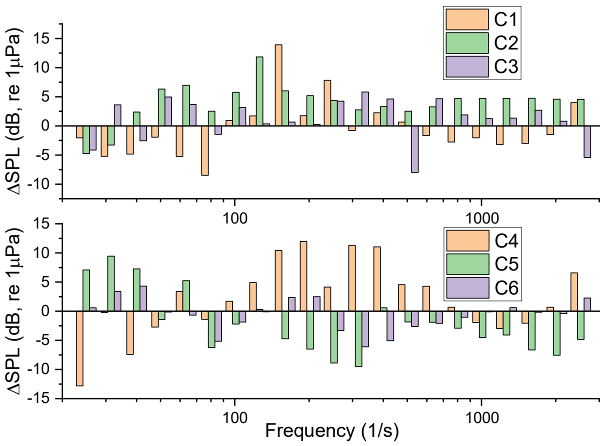

FIGURE 16: FAR-FIELD 3RD OCTAVE BAND ΔSPL SPECTRA FOR CONDITIONS C1-C6 (POSITIVE Y-AXIS DENOTES NOISE REDUCTION BY TUB DESIGN)

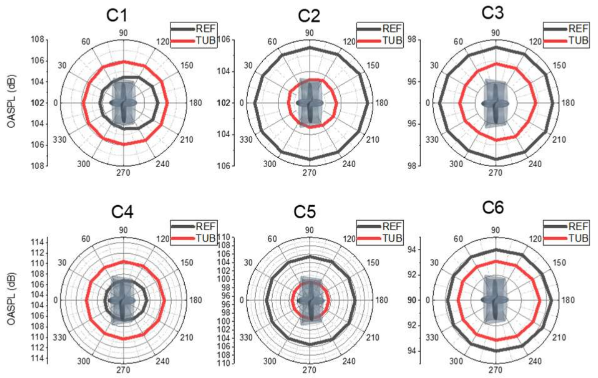

FIGURE 17: OASPL DIRECTIVITY PLOTS FOR ALL TEST CONDITIONS C1-C6

ACKNOWLEDGEMENTS

The funding support from BAE systems plc. (Ref: MEIR PhD 16) and the Royal Society (RGS\R1\191167) is greatly appreciated and acknowledged. Results were obtained using the ARCHIE-WeSt High-Performance Computer (www.archie-west.ac.uk) based at the University of Strathclyde.

REFERENCES

[1] Thomsen, F., Mendes, S., Bertucci, F., Breitzke, M., Ciappi, E., Cresci, A. Debusschere, E., Ducatel, C., Folegot, F., Juretzek, C., Lam, F-P., O'Brien, J., dos Santos, M. E. (2021) Addressing underwater noise in Europe: Current state of knowledge and future priorities. Kellett, P., van den Brand, R., Alexander, B., Muniz Piniella, A., Rodriguez Perez, A., van Elslander, J., Heymans, J. J. [Eds.] Future Science Brief 7 of the European Marine Board, Ostend, Belgium. ISSN: 2593-5232

[2] Kaplan, M.B. and Solomon, S. (2016). A coming boom in commercial shipping? The potential for rapid growth of noise from commercial ships by 2030. *Marine Policy*, *73*, pp.119-121.

[3] IMO, M., (2014). Guidelines for the reduction of underwater noise from commercial shipping to address adverse impacts on marine life. *MEPC*.

[4] Cruz, E. Lloyd, T., Bosschers, J., Lafeber, F.H., Vinagre, P. Vaz, G. (2021). Study on inventory of existing policy, research and impacts of continuous underwater noise in Europe. EMSA report EMSA/NEG/21/2020. WavEC Offshore Renewables and Maritime Research Institute Netherlands.

[5] Bertschneider, H., Bosschers, J., Choi, G.H., Ciappi, E., Farabee, T., Kawakita, C. and Tang, D. (2014). Specialist committee on hydrodynamic noise. *Final report and recommendations to the 27th ITTC. Copenhagen, Sweden*, *45*.

[6] Carlton, J. (2018). *Marine propellers and propulsion*. Butterworth-Heinemann.

[7] Fish, F.E. and Battle, J.M. (1995). Hydrodynamic design of the humpback whale flipper. *Journal of morphology*, *225*(1), pp.51-60.

[8] Miklosovic, D.S., Murray, M.M., Howle, L.E. and Fish, F.E. (2004). Leading-edge tubercles delay stall on humpback whale (Megaptera novaeangliae) flippers. *Physics of fluids*, *16*(5), pp.L39-L42.

[9] Custodio, D., Henoch, C. and Johari, H. (2018). Cavitation on hydrofoils with leading edge protuberances. *Ocean Engineering*, *162*, pp.196-208.

[10] Weber, P.W., Howle, L.E. and Murray, M.M. (2010). Lift, drag, and cavitation onset on rudders with leading-edge tubercles. *Marine Technology and Sname News*, *47*(01), pp.27-36.

[11] Shi, W., Atlar, M., Rosli, R., Aktas, B. and Norman, R. (2016). Cavitation observations and noise measurements of horizontal axis tidal turbines with biomimetic blade leading-edge designs. *Ocean engineering*, *121*, pp.143-155.

[12] Stark, C., Shi, W. and Atlar, M. (2021). A numerical investigation into the influence of bio-inspired leading-edge tubercles on the hydrodynamic performance of a benchmark ducted propeller. *Ocean Engineering*, *237*, p.109593.

[13] Stark, C. and Shi, W. (2021, June). The influence of leading-edge tubercles on the sheet cavitation development of a benchmark marine propeller. In *40th International Conference on Ocean, Offshore and Arctic Engineering: OMAE 2021*.

[14] Stark, C. and Shi, W. (2021, June). The influence of leading-edge tubercles on the hydrodynamic performance and propeller wake flow development of a ducted propeller. In *The 31st (2021) International Ocean and Polar Engineering Conference: ISOPE-2021*.

[15] Stark, C. and Shi, W. (2021). Hydroacoustic and hydrodynamic investigation of bio-inspired leading-edge tubercles on marine-ducted thrusters. *Royal Society open science*, *8*(9), p.210402.

[16] Stark, C., Shi, W. and Troll, M. (2021). Cavitation funnel effect: bio-inspired leading-edge tubercle application on ducted marine propeller blades. *Applied Ocean Research*, *116*, p.102864.

[17] Lidtke, A.K., Lloyd, T. and Vaz, G. (2019). Acoustic modelling of a propeller subject to non-uniform inflow. In *Sixth International Symposium on Marine Propulsors, SMP2019, Rome, Italy*.

[18] ITTC—Recommended Procedures and Guidelines (2014). Practical guidelines for ship CFD.

[19] Sezen, S., Atlar, M., Fitzsimmons, P., Sasaki, N., Tani, G., Yilmaz, N. and Aktas, B. (2020). Numerical cavitation noise prediction of a benchmark research vessel propeller. *Ocean Engineering*, *211*, p.107549.

[20] Celik, I.B., Ghia, U., Roache, P.J. and Freitas, C.J. (2008). Procedure for estimation and reporting of uncertainty due to discretization in CFD applications. *Journal of fluids Engineering-Transactions of the ASME*, *130*(7).

[21] Moulijn, J., Bosschers, J., Tornros, S., Schreiber, C., Grassi, D., Goedbloed, I. and Bijlard, M., Validation studies of a boundary element method for ducted propellers. In *Sixth International Symposium on Marine Propulsors, SMP* (Vol. 19).

[22] Ianniello, S., Muscari, R. and Di Mascio, A. (2013). Ship underwater noise assessment by the acoustic analogy. Part I: nonlinear analysis of a marine propeller in a uniform flow. *Journal of marine Science and technology*, *18*(4), pp.547-570.